Journal of Corrosion and Materials
www.corromat.com

J. Corros. Mater. (2025) 4(1), 63–74.

Cr–Mo-Enriched Boundary Networks Govern Repassivation and Intergranular Cracking of 316L Stainless Steel in Oxygenated High-Temperature Water

Kostya Trachenko[1,*], Antoine Laurent[2]

[1] *School of Physical and Chemical Sciences, Queen Mary University of London, London E1 4NS, United Kingdom*

[2] *Department of Mechanical Engineering, INSA Lyon, 20 Avenue Albert Einstein, 69621 Villeurbanne Cedex, France.*

[*] Corresponding author: k.trachenko@qmul.ac.uk

[*] antoinelaurent037@gmail.com

(Received: 12 February 2025. Received in revised form: 4 May 2025. Accepted: 17 May 2025. Published online: 30 June 2025.)

Abstract

The cracking of 316L stainless steel in oxygenated high-temperature water is controlled by a local competition between film failure, intergranular oxidation, and fast chemical healing at the crack tip. The comparison of three types of 316L stainless steel — wrought conventional 316L stainless steel, cold-worked wrought 316L stainless steel, and laser powder-bed-fused 316L stainless steel — reveals that the presence of defects cannot explain the penetration of cracks. Cold working introduces the dislocation density of 1.6×10^{14} m^{-2} and the low-angle boundary fraction of 44.2%. Nevertheless, it provides the deepest average intergranular crack length of 515 nm and the largest isolated event of 2000 nm. Laser powder-bed fusion leads to the largest dislocation density of 1.1×10^{14} m^{-2} and the largest low-angle boundary fraction of 65.4%. However, laser powder-bed fused 316L stainless steel restricts the average crack length to 278.8 nm when applying the highest target stress of 520.6 MPa during the longest exposure of 744.4 h. The discriminating factor is the chemical state of the boundaries: deformation cells of the cold worked sample are poor in chromium and molybdenum; while solidification cell walls of the printed sample have Cr/Mo-enriched and Fe-depleted regions. A repassivation index related to the supply of boundary connectivity is defined by the following parameters: Cr–Mo inventory, low-angle boundary fraction, dislocation density, Cr/Mo cell-wall chemistry, mechanical severity, and grain-boundary segregation energies. For conventional wrought 316L stainless steel, cold-worked 316L stainless steel, and laser powder-bed-fused 316L stainless steel, the values of this index are 32.4, 22.4, and 71.4, respectively. The manipulations by substitutions of alloying elements reveal that eliminating the Cr/Mo cell-wall chemistry reduces the value for printed 316L stainless steel from 71.4 to 21.0, while introducing such chemistry into the cold-worked 316L sample results in an increase in the value from 22.4 to 70.9. Consequently, the structure of cracking is controlled by chemically supplied boundary connectivity rather than by overall defect concentration or total molybdenum concentration.

Keywords: 316L stainless steel; stress corrosion cracking; laser powder-bed fusion; Cr–Mo segregation; grain boundary; repassivation; high-temperature water

1. Introduction

The corrosion resistance of austenitic 316L stainless steel in aqueous solutions results from the presence of a passive film rich in chromium, but the same alloy can develop a stress corrosion cracking mode in the presence of tensile strain, oxidizing water environment, grain-boundary sensitivity, and rupture of the film in cycles. Service in high-temperature water environments makes the competition between corrosion protection and cracking even more pronounced since oxidation and diffusion processes proceed faster at the cracks tips and stresses are concentrated in grain-boundaries. Intergranular cracking in Fe–Ni–Cr alloys has long been known to be strongly connected to grain-boundary chemistry, not alloy composition itself [1]. Oxygen dissolved in water changes the stress corrosion cracking response of cold worked 316L in a simulated pressurized-water-reactor environment [2]. Recent reviews on austenitic stainless steels emphasize the significance of cold work in primary water cracking [3]. Constant-load testing reveals the initiation mechanism of cold worked 316L in an oxygenated high-temperature water environment [4].

The slip-dissolution and repassivation mechanism still provides a good physical description of the phenomenon. Modern interpretation of the slip-dissolution model clarifies how repeated film rupture enables stress-corrosion cracking [5]. Application of the slip-dissolution model to stainless steel demonstrates the significance of competition between film dissolution and repassivation [6]. Sensitivity analysis further shows that prediction of crack growth is sensitive to stability of the model inputs [7]. The initial stage of crack growth takes place when local plasticity destroys the protective film and exposes new metal to the environment. If dissolution and oxidation outpace oxide film healing, the crack grows. When the compact film enriched with chromium re-forms, the crack propagation stops. Chromium plays an important role in the process. Addition of molybdenum can decrease the stress corrosion cracking susceptibility of lean austenitic stainless steels [8]. Theory of

grain-boundary segregation further explains the effect of solute atoms on local cohesion and reactivity [9]. The route for transport of chromium and molybdenum to the crack tip, therefore, is as important as wt.% content of the elements.

Laser powder-bed fusion changes the route due to creation of a non-equilibrium microstructure different from wrought 316L stainless steel. Rapid solidification leads to sub-micrometer cellular walls, low angle boundary networks, dislocation tangles, solute partitioning and residual strain. Dislocation network of additively manufactured steel enables overcoming the conventional strength–ductility trade-off [10]. Hierarchically printed 316L combines high strength with retained ductility [11]. Microscopy helps to identify the origin of dislocation structures formed in additive manufacturing process [12]. Cellular strengthening and thermal stability studies explain the behavior of these structures in the course of subsequent heat treatments [13]. Corrosion properties, however, can be more specific. Heat treatment affects both microstructure and corrosion response of selectively melted 316L [14]. Passivity studies prove that surface state of additively manufactured steel is different from conventionally treated stainless steel [15]. Comparison of additively manufactured materials correlates these differences with microstructure specifics [16]. High-temperature-water experiments further demonstrate how heat treatment influences corrosion behavior of printed 316L [17]. Recent comparison of laser powder-bed fusion and direct energy deposition confirms that post-build heat treatment changes passivity-related microstructure [18]. Dislocation rich walls, therefore, can promote fast transport of protective solutes, but can accumulate strain or create electrochemical contrast.

An important distinction is necessary between two seemingly similar cellular structures. Cyclic deformation of wrought 316L creates evolving dislocation structures through slip rearrangement [19]. Cyclic deformation studies demonstrate how planar slip creates dislocations of different type [20]. Thus, cold working creates dislocation induced cells with increased dislocation density without formation of solidification induced wall chemistry enriched with Cr/Mo. Selective laser melting, on the contrary, creates metastable cellular microstructure in the course of rapid solidification [21]. Even micro-laser powder-bed fusion can create two cellular structures in printed 316L [22]. Therefore, laser powder-bed fusion creates solidification cells with Cr and Mo segregation to walls owing to rapid partitioning. The corrosion function of the cell wall should be determined by its chemistry and not by morphology alone.

The objective of this manuscript is to determine whether shallow cracking response of laser powder-bed-fused 316L in oxygenated high-temperature water depends on chemically supplied grain boundary connectivity, and not on low defect density, higher bulk molybdenum content, or milder loading conditions. The analysis involves three material states: conventional wrought 316L, cold worked wrought 316L, and stress relieved laser powder-bed-fused 316L. The analysis uses alloy composition, slow strain rate tests, microstructural quantification, crack depth determination, crack tip composition, AFM/SKPFM contrast and DFT segregation energies to calculate repassivation index supplied by grain-boundaries. This index is then compared to crack penetration depth and substitution experiments that isolate the effect of Cr/Mo wall chemistry, molybdenum content and mechanical stress.

2. Material records and environmental exposure

The tabulated data refers to the three conditions of 316L stainless steel studied by Zhou et al. [23]. The standard wrought condition is marked CM, the 10% cold worked condition is marked CW, and the stress relieved laser powder bed fused condition is marked L-PBF. The fabricated alloy was produced using laser powder bed fusion followed by stress relief annealing at 650 °C for 2 h in an argon atmosphere. The current study is highly appropriate to distinguish between the effects of cell structure formation due to plastic strain and cellular solidification, since the cold-worked condition has a high dislocation density but no chromium/molybdenum wall enrichment, whereas the printed condition has both.

Table 1: Microstructural state variables.

Condition	Grain size (μm)	LAGB (%)	Dislocation density (m^{-2})	Cells	Cr/Mo at cells
CM	73.8 ± 25.3	1.3	9.6×10^{12}	No	No
CW	72.0 ± 25.0	44.2	1.6×10^{14}	Yes	No
L-PBF	82.7 ± 23.4	65.4	1.1×10^{14}	Yes	Yes

The entries in Table 1 illustrate why such a one-dimensional ordering is insufficient. CW has the highest dislocation density, while L-PBF has the highest low-angle boundary density and the unique Cr/Mo-rich cell walls. CM represents a low connectivity baseline, with only 1.3% low-angle boundaries and no enriched cell wall composition. Thus, the three states distinguish between the level of deformation structure and its chemical capability to provide protection by supplying solute.

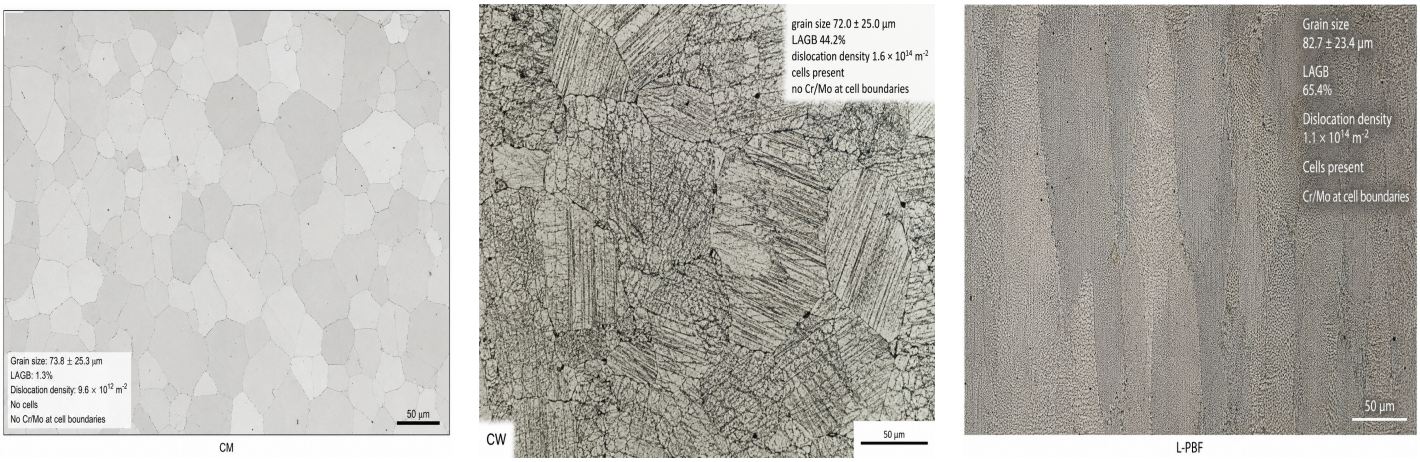

(a) CM. (b) CW. (c) L-PBF.

Figure 1: Material-state micrographs.

Metallographic sections in Fig. 1 emphasize the numerical differences in Table 1. The standard wrought state is characterized mainly by equiaxial grains, without much low-angle subdivision. The cold-worked state is characterized by heavy subdivision due to deformation bands and cells. The printed state is characterized by columns and cells, with the distinction that the cells in this case are related to wall chemistry of Cr/Mo.

Table 2: Chemistry and SSRT conditions.

Condition	Cr (wt.%)	Mo (wt.%)	Nominal strain (%)	Target stress (MPa)	Actual strain (%)	Duration (h)
CM	17.3	2.60	12.5	327.0	10.0	694.5
CW	17.3	2.60	12.5	497.6	9.9	694.4
L-PBF	17.9	2.33	13.4	520.6	9.8	744.4

Table 2's entries for chemistry and loading preclude two straightforward reasons why L-PBF has a faster response to cracking. First, while the powder-printed material has slightly higher amounts of chromium when compared to its wrought counterpart, it has lower levels of molybdenum. Second, it was subjected to the highest target stress for the longest time period. The shallower cracking depth of the L-PBF material can thus be attributed to local distribution of Cr/Mo.

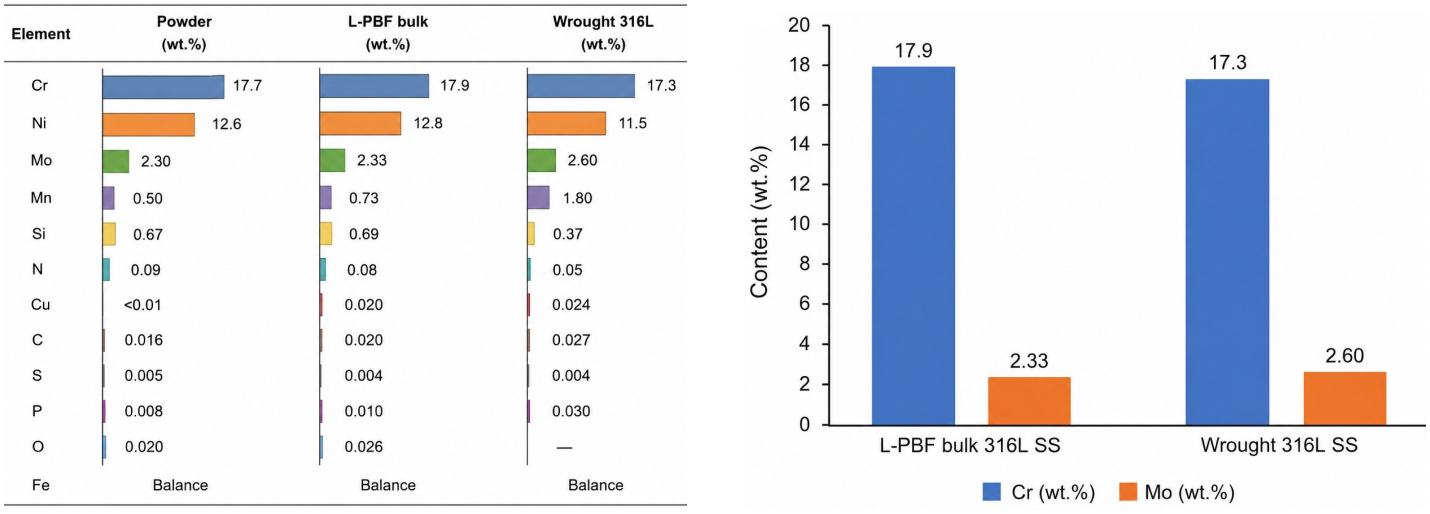

(a) Alloy entries. (b) Cr–Mo balance.

Figure 2: Alloy chemistry.

The chemical analysis shown in Figure 2 brings out the molybdenum point rather clearly: wrought 316L has 2.60 wt.% Mo, while L-PBF bulk has 2.33 wt.% Mo. Under the assumption that total amount of molybdenum is the dominating factor, the wrought situation should be resistant to crack propagation at least as much as the printed situation. However, the hierarchy needs to take into account the location of the Mo at cell wall and grain boundary level.

Material	Nominal strain (%)	Target stress (MPa)	Actual strain (%)	Duration (h)
CM	12.5	327.0	10.0	694.5
CW	12.5	497.6	9.9	694.4
L-PBF	13.4	520.6	9.8	744.4

Figure 3: SSRT exposure.

The exposure situation in Figure 3 shows that all three materials are exposed to a very demanding environment: 325 °C, 15.5 MPa, approximately 2 ppm of dissolved oxygen and 5×10^{-8} s^{-1} strain rate. L-PBF reached 520.6 MPa and 744.4 h, compared with 327.0 MPa and 694.5 h for CM. The printed material's lower crack depth is therefore not an artifact of reduced stress or shorter time.

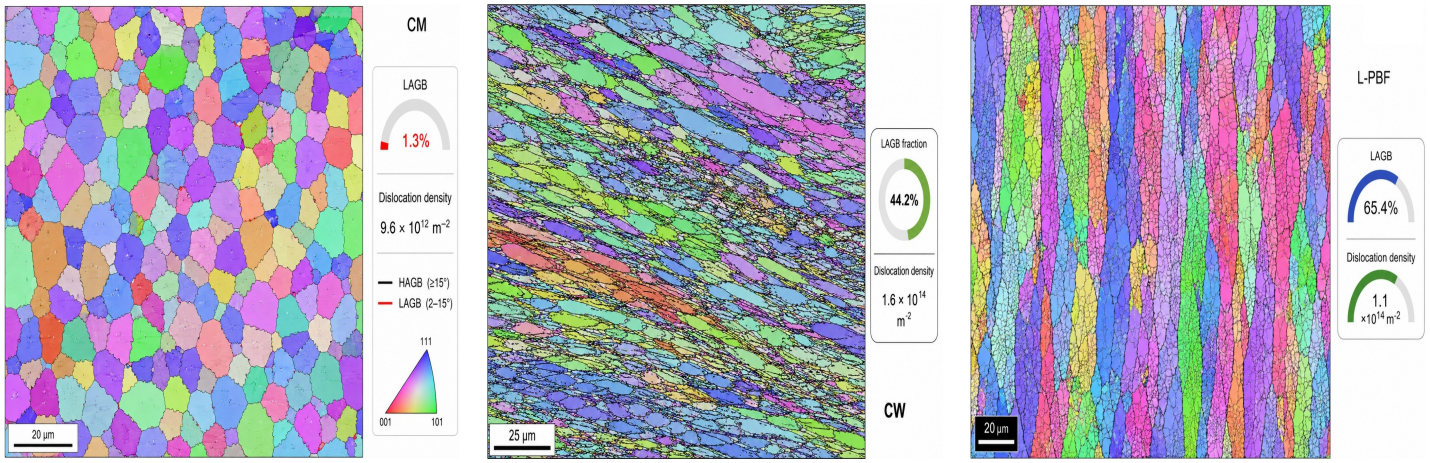

(a) CM. (b) CW. (c) L-PBF.

Figure 4: Boundary connectivity.

Maps presented in Figure 4 depict the spatial aspect of the problem. CM contains only a few internal boundaries and their connections. CW contains many deformation features and is highly substructured. L-PBF possesses a more connected network of printed sub-grain and cellular walls. The effectiveness of this network as a protective feature depends on the chemical nature of it, which is why Figure 5 is crucial for understanding.

The cellular comparison provided in Figure 5 differentiates between the morphology and corrosive properties. The deformation cells of CW are roughly 160 nm and have no enrichment of Cr/Mo wall chemistry. Printed cells are approximately 600 nm with walls of 50 nm. The elemental maps reveal enrichment of Cr/Mo and depletion of Fe at the printed wall, thus the printed wall is a local chemical reservoir, while the cold worked one is a deformation product.

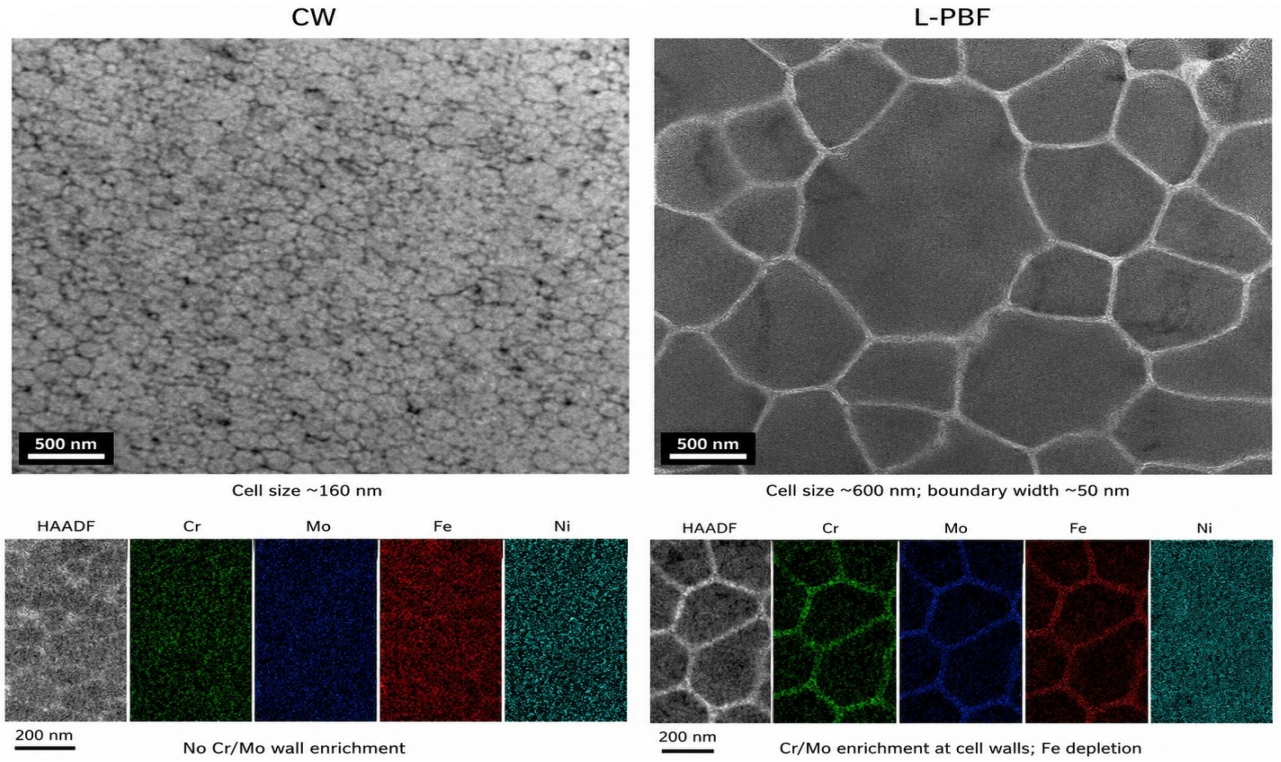

Figure 5: Cell-wall chemistry.

3. Boundary-supplied repassivation calculation

The boundary supplied repassivation index reflects the competition between favorable boundary supply of solutes and two adverse parameters: mechanical severity and connectivity of defects without Cr/Mo wall chemistry. Five quantities are used in the calculation. First one is the Cr-Mo inventory term R_i that weights Cr more heavily because of Cr rich oxide formation being the main repair process, but keeps Mo in account due to its effect on localized corrosion and boundary cohesion:

$$R_i = 0.60\frac{C_{\mathrm{Cr},i}}{C_{\mathrm{Cr,max}}} + 0.40\frac{C_{\mathrm{Mo},i}}{C_{\mathrm{Mo,max}}}. \tag{1}$$

This factor by itself will not be sufficient to determine the final order, because in this case, the value of R_i in L-PBF is smaller than that of the wrought alloy, due to less amount of molybdenum in the former. Hence, the inventory factor will serve only as the initial chemical potential.

The second factor, K_i, includes both the low-angle boundary fraction and dislocation density:

$$K_i = \frac{1}{2}\frac{f_{\mathrm{LAGB},i}}{f_{\mathrm{LAGB,max}}} + \frac{1}{2}\frac{\log_{10}(\rho_i) - \log_{10}(\rho_{\min})}{\log_{10}(\rho_{\max}) - \log_{10}(\rho_{\min})}. \tag{2}$$

However, the dislocation term in logarithmic form helps to avoid having the maximum dislocation density dominate the equation. CW and L-PBF get high connectivity scores, yet the third term tells whether such connectivities are chemically active or chemically inactive.

The third parameter, G_i, describes the affinity of Cr–Mo pairs to occupy boundary positions:

$$G_i = \frac{C_{\mathrm{Cr},i}|E_{\mathrm{seg}}^{\mathrm{Cr3}}| + C_{\mathrm{Mo},i}|E_{\mathrm{seg}}^{\mathrm{Mo3}}|}{\max\left(C_{\mathrm{Cr}}|E_{\mathrm{seg}}^{\mathrm{Cr3}}| + C_{\mathrm{Mo}}|E_{\mathrm{seg}}^{\mathrm{Mo3}}|\right)}. \tag{3}$$

Cr3 and Mo3 indicate the stronger enriched boundary conditions. The term endows molybdenum a great impact due to its larger segregation energy compared to its bulk concentration.

The chemical connectivity term is defined by

$$S_i = \chi_i K_i G_i, \tag{4}$$

with $\chi_i = 1$, if Cr/Mo enriched cell walls exist and $\chi_i = 0$, if they do not. This is the main difference between CW and L-PBF. Both have highly connected boundaries, but only L-PBF has Cr/Mo enriched cell walls.

Mechanical severity and unsupplied connectivity terms are defined by

$$M_i = \frac{\sigma_{t,i}}{\sigma_{t,\max}} \frac{t_i}{t_{\max}} \frac{\varepsilon_{a,i}}{\varepsilon_{a,\max}}, \tag{5}$$

$$U_i = (1 - \chi_i) K_i. \tag{6}$$

The first term penalizes high stress, long exposure time, and comparable level of strain. The second term penalizes dense boundaries that lack chemical contribution of Cr/Mo due to CW reinforcement. This is crucial when CW is treated realistically, since the resulting boundary cracks increase the probability of film rupture without contributing any Cr/Mo-rich healing chemistry.

The final boundary repair capability is then

$$B_i = 100 \frac{0.40 R_i (1 + 0.10 K_i) + 0.60 S_i}{1 + 0.35 M_i + 0.70 U_i}. \tag{7}$$

The numerator weights chemical connectivity over bulk availability, because stress corrosion cracking propagates via boundary crack tips. The denominator penalizes mechanical severity and unsupplied defects. It is not a fracture mechanics constant, but just a convenient way of summarizing three measured material properties in terms of the parameters that are most directly related to repassivation at crack tips.

4. Crack penetration and crack-tip chemistry

The crack behavior serves as a test to challenge the assumption that chemical connectivity, and not just density of defects, determines the hierarchy of cracking. CM exhibits moderately deep cracks, CW exhibits deeper and more varied IG cracks, while L-PBF has the least deep cracks. This observation is incompatible with the assumption that "the higher the number of dislocations, the better passivation," because CW has the highest dislocation density and the worst crack behavior.

Table 3: Intergranular crack response.

Condition	Average depth	Depth character	Cr/Mo at cells	Crack-tip interpretation
CM	364.9 nm	Mostly below 550 nm	No	Bulk passivity without a strong internal Cr/Mo route
CW	515 nm	Events above 2000 nm	No	Dense deformation defects without local chemical supply
L-PBF	278.8 nm	Mostly below 350 nm	Yes	Cr/Mo cell walls support near-tip repair

From Table 3, the lowest crack depth is found to be under the condition where high connectivity exists along with the Cr/Mo wall chemistry. The L-PBF technique results in an average crack depth of 278.8 nm despite the fact that it has neither the highest bulk Mo content nor the most moderate stress condition. CW results in the highest average crack depth of 515 nm and has values more than 2000 nm in some instances.

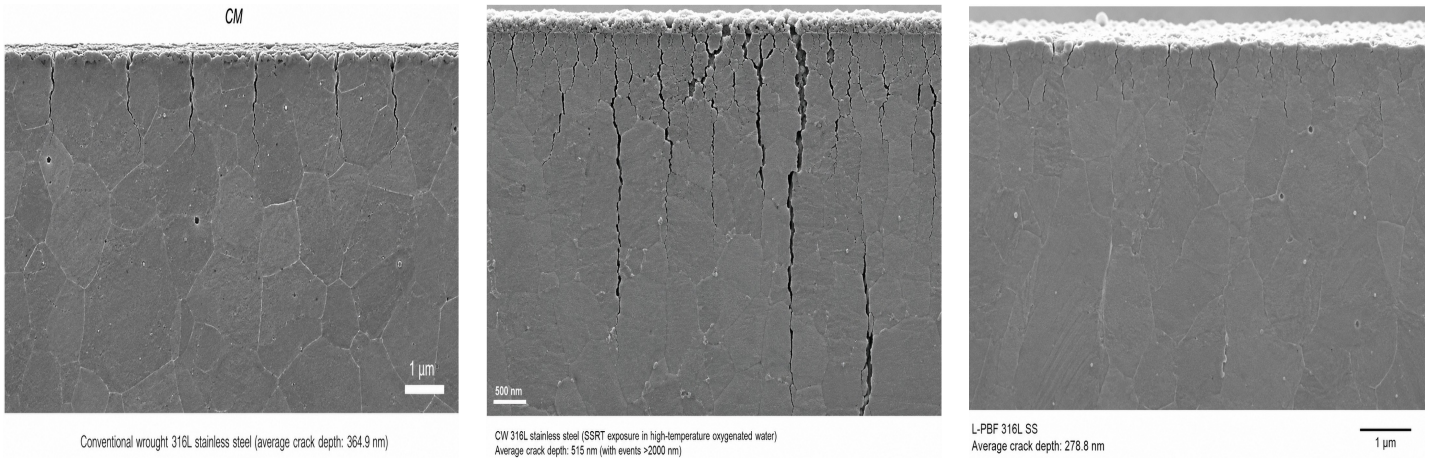

(a) CM. (b) CW. (c) L-PBF.

Figure 6: Intergranular crack penetration.

The images in Fig. 6 give a graphical illustration of the tabulated crack depth data. In CM, there are quite shallow intergranular cracks that exist beneath the oxidized surface layer. In CW, there are many more cracks, which are deeper,

including long cracks that extend all the way through the deformation affected grain boundaries. L-PBF has fewer, but shallower cracks that are predominantly at the surface level. It is particularly significant to compare CW with L-PBF since both have a high defect density.

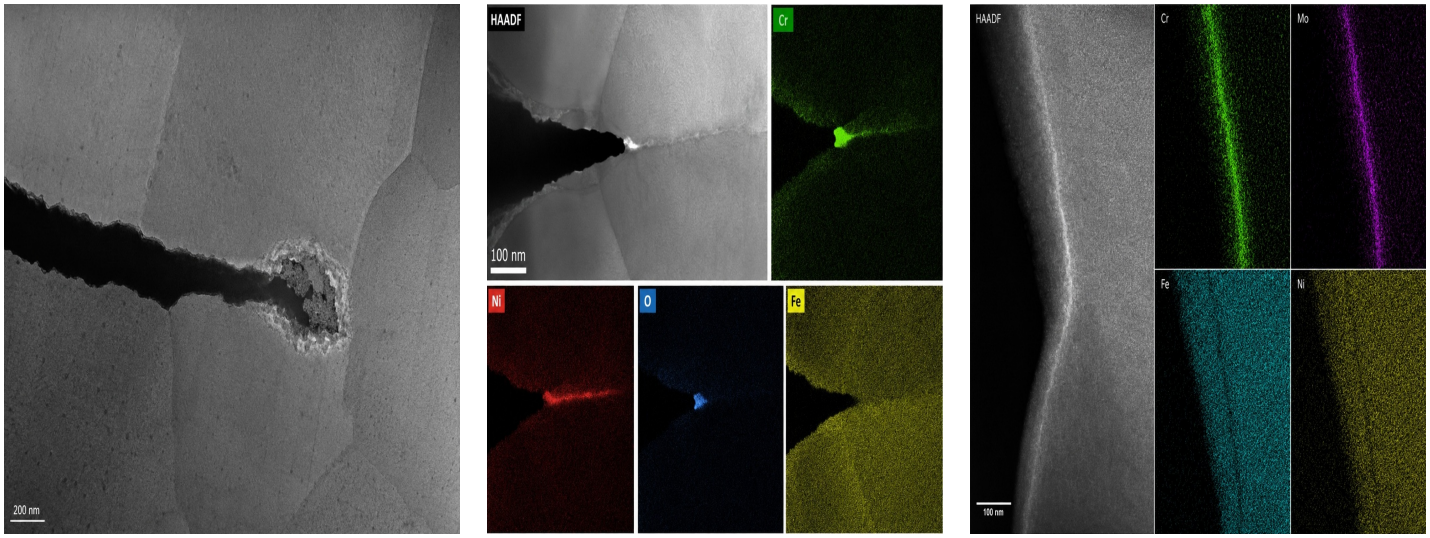

(a) HAADF. (b) Cr–Ni–O–Fe. (c) Cr–Mo band.

Figure 7: Crack-tip elemental contrast.

From the crack-tip maps shown in Figure 7, it can be seen that there is the chemistry behind why the L-PBF cracks have been shallow. This involves the existence of an oxide rich in Cr in the oxidized crack tip region, an oxide rich in Ni migrating up to around 60 nm from the crack front, and a grain-boundary oxide rich in Cr and Mo close to the crack front. This last one consists of a 10 nm wide boundary core with an enriched area of more than 40 nm.

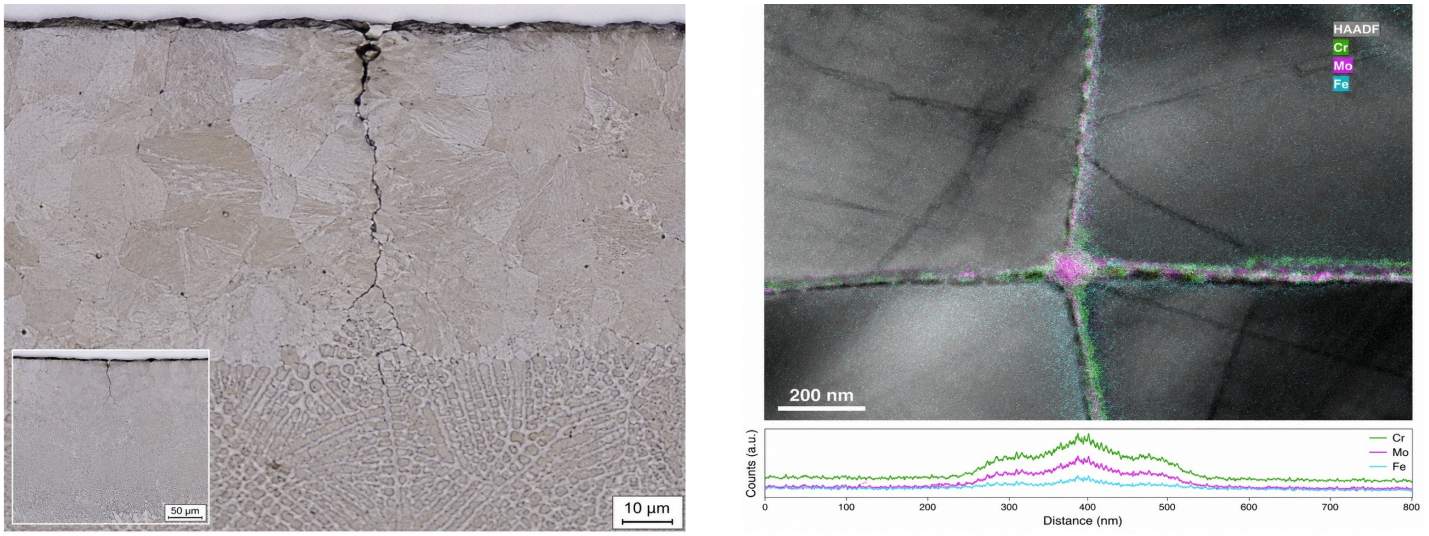

(a) Subsurface crack line. (b) Cr/Mo junction.

Figure 8: Subsurface GB-cell junction.

The sub-surface data in Fig. 8 relate crack-tip chemistry to the printed cellular architecture. In particular, there is a junction between the cell-wall grain boundary and another grain boundary 1.2 μm beneath the surface, where there is enrichment of Cr/Mo at both the junction and the nearby grain boundary. This suggests that the printed cellular wall can chemically connect to a segment of the grain boundary that participates in intergranular cracking.

The surface characterization results shown in Fig. 9 reveal that the printed cellular walls are also topographically and electrochemically distinct. The height of the printed sample was between -45.9 to 55.1 nm after etching, while the Volta potential of the printed sample varied between -27.3 to 28.4 mV. Driving forces due to solute diffusion can link the process of solute segregation to localized stress evolution [24]. Modeling efforts have been made in coupling stress-diffusion behavior and shown the effect of grain-boundary segregation on embrittlement [25]. Electrochemical characterization has established that additive manufacturing changes the passive behavior of 316L [16]. These observed differences are thus compatible with

local compositional variations between cell walls and also offer an explanation for the participation of Cr/Mo-bearing cell walls in solute transfer at high temperatures.

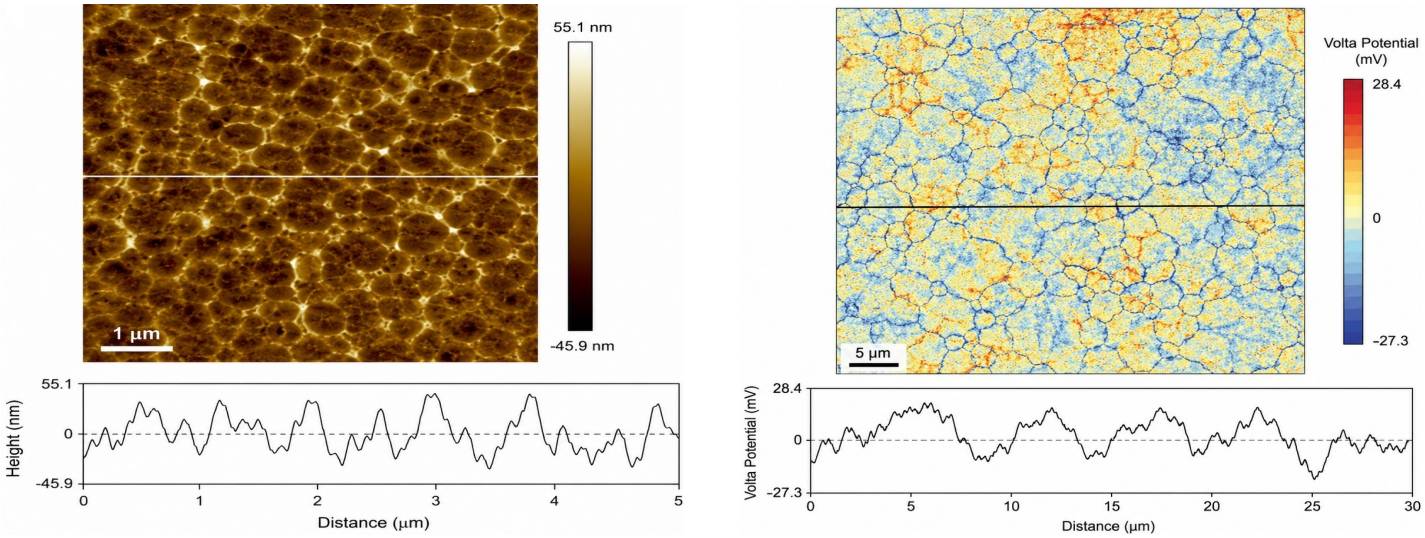

(a) Topography. (b) Potential.

Figure 9: AFM/SKPFM cellular-wall contrast.

5. Energetics of Segregation and Contribution of Molybdenum

The segregation energy values explain on an atomic level why molybdenum has an appreciable impact even when the bulk concentration is very small. The grain boundary replacement energies for chromium are slightly negative; those for molybdenum are highly negative and those for nickel are positive. The values of the energies thus suggest that chromium and molybdenum, but not nickel, are preferred to be segregated at the boundaries. This is in line with the crack tip maps, where the enrichment of Cr/Mo is a key chemical marker.

Table 4: Boundary segregation energies.

Elemental case	Boundary occupation (%)	E_{seg} (eV atom^{-1})
Cr1	12.5	−0.024
Cr3	37.5	−0.026
Ni1	12.5	0.120
Ni3	37.5	0.102
Mo1	12.5	−0.096
Mo3	37.5	−0.186

Table 4 clearly indicates that molybdenum has the highest value of the boundary preference compared to other elements discussed in this table. The boundary energy for Mo3 is −0.186 eV/atom which is significantly lower than the boundary energy of Cr3 (−0.026 eV/atom). Nickel shows positive values meaning that it has no boundary enrichment driving force.

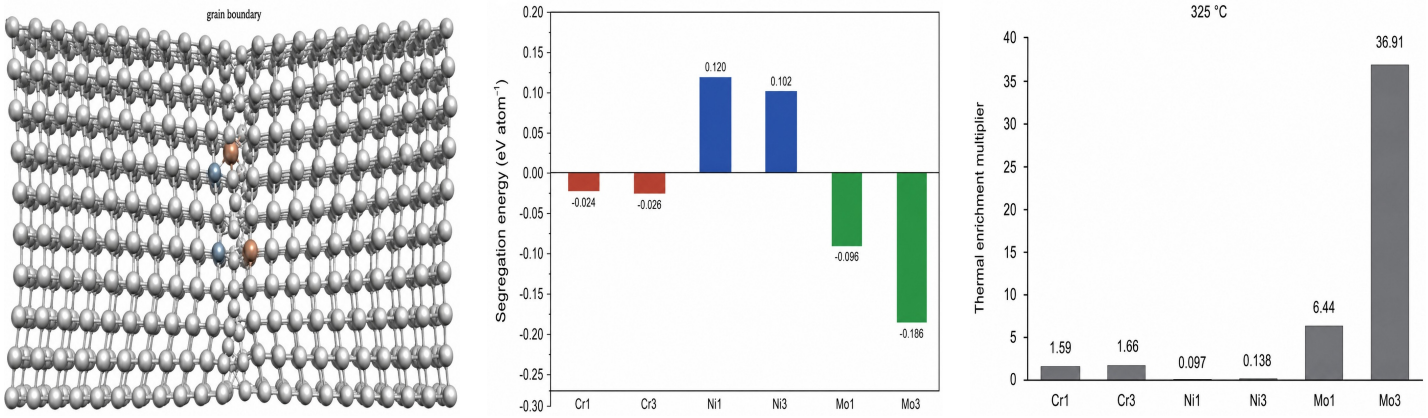

(a) Boundary slab. (b) Energy. (c) Multiplier.

Figure 10: Segregation energetics.

Figure 10 shows the energetics that translate the values in Table ?? into an easily understandable chemical ranking. The enrichment factors at 325 °C are 1.59 for Cr1, 1.66 for Cr3, 0.097 for Ni1, 0.138 for Ni3, 6.44 for Mo1, and 36.91 for Mo3. This means that the molybdenum atoms have a disproportionate effect on boundary reconstruction since they are thermodynamically preferred at enriched boundary sites rather than because they are plentiful.

6. Index values and controlled substitutions

CM alloy has a higher inventory of Cr–Mo than CW due to its wrought state, but a very low connected boundary index value. CW alloy has high connectivity, but its chemical term value is zero and the deficiency defect value is high. The L-PBF alloy has a slightly lower inventory of Cr–Mo compared to the wrought alloy but possesses high connectivity along with a nonzero chemical term value.

Table 5: Boundary repair index.

Condition	R	K	G	S	M	U	B
CM	0.980	0.010	1.000	0.000	0.586	0.010	32.4
CW	0.980	0.838	1.000	0.000	0.883	0.838	22.4
L-PBF	0.958	0.933	0.963	0.899	0.980	0.000	71.4

The elements from Table 5 show why CW gets a low final index. CW does not have flaws but is penalized because of its highly connected structure that is not chemically supplied. L-PBF gets the largest value because the element S equals 0.899 while the element U is equal to 0.

Condition	R	K	G	S	M	U	B
CM	0.980	0.010	1.000	0.000	0.586	0.010	32.4
CW	0.980	0.838	1.000	0.000	0.883	0.838	22.4
L-PBF	0.958	0.933	0.963	0.899	0.980	0.000	71.4

Figure 11: Boundary repair index.

The most explicit numerical representation can be found in the tabulated figure 11. CM gets the value 32.4, CW gets 22.4, and L-PBF gets 71.4. Even though the printed sample has the largest value of mechanical severity, 0.980, it still reaches the largest final index due to the chemical supply of its connected boundaries. Such a ranking coincides with the rankings based on crack depth measurements.

Table 6: Controlled substitutions.

Condition	Calculation condition	B
L-PBF	Measured values retained	71.4
L-PBF	Cr/Mo cellular chemistry removed	21.0
CW	Cr/Mo cellular chemistry assigned	70.9
L-PBF	Target stress changed from 520.6 MPa to 327.0 MPa	78.9
L-PBF	Mo term removed from the calculation	40.3

Substitutions in Table 6 show that the controlling variable is identified through those substitutions. Removal of the Cr/Mo wall chemistry brings down the L-PBF value to 21.0, close to the CW limit. Addition of Cr/Mo chemistry to the

cold-worked network boundary elevates the value to 70.9. In the substitution of the removal of the molybdenum, the L-PBF value is reduced to 40.3. This proves that the presence of Mo makes a substantial contribution to the boundary repair.

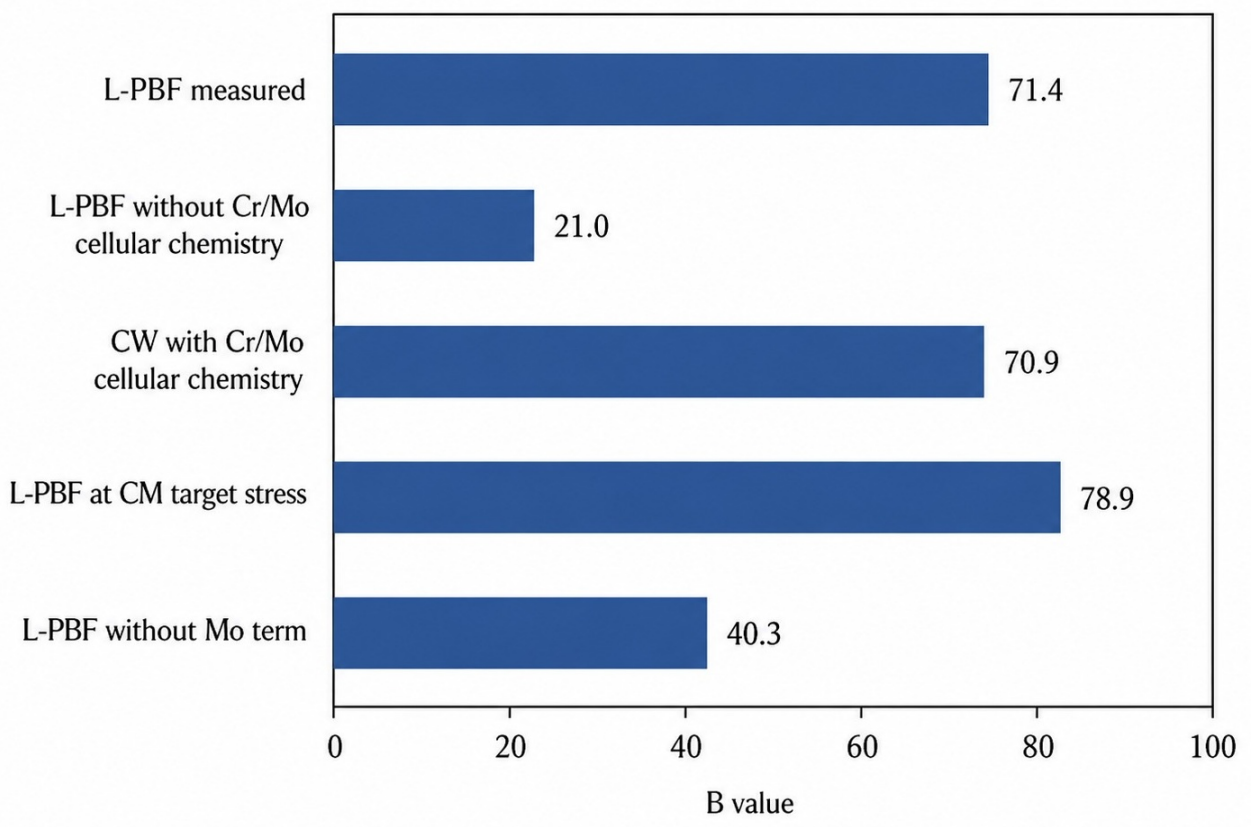

Figure 12: Controlled substitutions.

The bar graph in Figure 12 depicts the fact that the most influential factor is the Cr/Mo wall chemistry and not the stress value modification. If the target stress for L-PBF is reduced to CM, then the index changes from 71.4 to 78.9, whereas eliminating Cr/Mo wall chemistry reduces it to 21.0. The chemical composition of the boundary network plays the critical role in distinguishing between good and bad cellular structure.

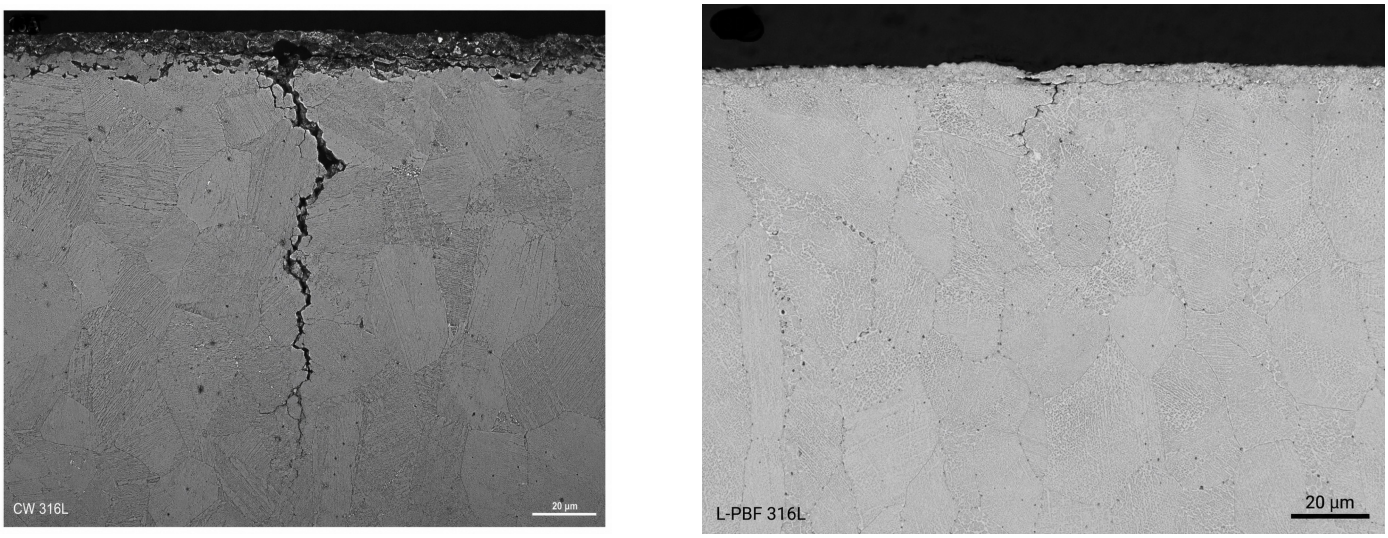

(a) CW. (b) L-PBF.

Figure 13: CW and L-PBF crack fields.

The last comparison in Figure 13 summarizes the research findings in terms of microstructure-based comparison. CW has deformation-affected boundaries and deeper cracks, whereas L-PBF has fine-printed cellular network and shallower crack. The difference lies in the chemical composition of the cellular walls rather than just in the number of defects. CW lacks Mo/Cr-enriched cell walls which could serve as boundary repair zone in proximity to the crack tip.

7. Implications for additively manufactured 316L stainless steel

This analysis demonstrates that cellularity is beneficial only when the cell walls are enriched with chromium and molybdenum. Cellularity caused by cold working increases defect density and strain without Cr/Mo wall enrichment. Cellularity resulting from laser powder-bed fusion is characterized by connection between dislocation-rich walls and Mo/Cr-enriched boundaries and grain-boundary crack paths. Crack growth tests under high-temperature water conditions prove that the performance of L-PBF 316L may be significantly different from the one of wrought steel [26]. Atmospheric stress-corrosion testing shows that build direction and heat treatments change the response of printed stainless steel [27]. Crack growth in high-temperature water at 288 °C proves the process dependency of the cracking behavior [28]. Studies of heat treatment reveal the connection between this variation and microstructural features responsible for passivity [18]. Tests on selectively melted 304L provide an example of printed cellular structure effecting stress-corrosion resistance in hydrogenated water [29].

Heat treatment should therefore be assessed in light of two factors: first, stress relief helps to decrease the mechanical potential of film rupture; second, homogenization may lead to loss of Cr/Mo enrichment of cell walls. Thermal aging studies of stainless steel weld metals prove the changes of environmentally assisted cracking behavior in high-temperature water due to microstructural evolution [30]. The desirable state of a specimen for high-temperature water treatment is not necessarily the one with lowest residual stress or highest defect density. It should be a balance where there is sufficient amount of boundary structure to transport the protective solutes, sufficient level of Cr/Mo enrichment and low mechanical severity to prevent repeated oxide film rupture.

Molybdenum is of special design interest since it has higher boundary preference in the enriched structures than chromium. Chromium is still the dominant passivation film element, but molybdenum greatly influences boundary chemistry and repassivation stability. The processing route which retains Mo-enriched cellular walls might offer stronger crack tip repair ability than the route increasing Mo content without placing it near the boundary network.

8. Conclusions

The research was aimed to test whether the shallow intergranular cracking of laser powder-bed-fused 316L stainless steel in oxygenated high-temperature water is influenced by defect density or chemically supplied boundary connectivity. The result shows that chemically supplied boundary connectivity is key factor. Conventional cold-worked 316L has highest dislocation density, 1.6×10^{14} m^{-2}, and highest fraction of low-angle boundaries, 44.2% but lacks Mo/Cr-enriched cell walls and gives the deepest cracks with average depth 515 nm. L-PBF has dislocation density of 1.1×10^{14} m^{-2}, highest low-angle boundary fraction 65.4% and Mo/Cr-enriched cellular walls and gives shallowest cracks, 278.8 nm despite highest target stress and exposure time.

The boundary-supplied repassivation index gives values of 32.4 for conventional 316L, 22.4 for cold-worked 316L and 71.4 for laser powder-bed-fused 316L. These values coincide with the crack depth hierarchy and indicate that the printed material does not benefit from higher Mo content in bulk and milder loading. Its advantage is based on the combination of spatial coupling between the connected cellular network and Cr/Mo enrichment.

Constrained substitutions provide quantitative answer to the materials question. Removal of Mo/Cr-enrichment of L-PBF reduces the index value from 71.4 to 21.0, while assignment of Mo/Cr-enrichment to cold-worked specimen increases the index from 22.4 to 70.9. Removal of molybdenum term lowers the value for the printed material to 40.3. Molybdenum acts as a strong boundary-active solute confirmed by its segregation energy -0.186 eV atom^{-1} and thermal enrichment multiplier 36.91 at 325 °C.

The practical lesson learned is that printed cellular structure cannot be evaluated based only on its morphology. The cell wall is effective in protection against stress corrosion cracking if it serves as a connector between Mo/Cr-rich reservoir and crack-related grain boundaries. Defect-rich boundaries without this chemical supply may deepen the cracks, while chemically supplied printed boundaries are capable to support repassivation and inhibit crack penetration.

Conflict of Interest

The author declares no competing financial or personal interests.

References

[1] Cowan, R. L. I. I., & Gordon, G. M. (1973). Intergranular Stress Corrosion Cracking and Grain Boundary Composition of Fe–Ni–Cr Alloys. Stress Corrosion Cracking and Hydrogen Embrittlement of Iron Base Alloys, 1023-1070.

[2] Zhang, L., & Wang, J. (2014). Effect of dissolved oxygen content on stress corrosion cracking of a cold worked 316L stainless steel in simulated pressurized water reactor primary water environment. Journal of nuclear materials, 446(1-3), 15-26.

[3] Ehrnstén, U., Andresen, P. L., & Que, Z. (2024). A review of stress corrosion cracking of austenitic stainless steels in PWR primary water. Journal of Nuclear Materials, 588, 154815.
[4] Wang, J., Zhu, T., Chen, K., Bao, Y., Ma, W., Zhang, M., ... & Zhang, L. (2022). Investigations on the SCC initiation behavior of cold worked 316 L in high temperature oxygenated water at constant loads. Corrosion Science, 203, 110336.
[5] Newman, R. C. (1994). Developments in the slip-dissolution model of stress corrosion cracking. Corrosion, 50(9), 682-686.
[6] Nakayama, T., & Takano, M. (1986). Application of a slip dissolution-repassivation model for stress corrosion cracking of AISI 304 stainless steel in a boiling 42
[7] Newman, R. C., & Healey, C. (2007). Stability, validity, and sensitivity to input parameters of the slip-dissolution model for stress-corrosion cracking. Corrosion Science, 49(10), 4040-4050.
[8] Ha, H. Y., Seo, W. G., Park, J. Y., Lee, T. H., & Kim, S. (2016). Influences of Mo on stress corrosion cracking susceptibility of newly developed FeCrMnNiNC-based lean austenitic stainless steels. Materials Characterization, 119, 200-208.
[9] Hofmann, S., & Leiĉek, P. (1996). Solute segregation at grain boundaries. Interface Science, 3(4), 241-267.
[10] Liu, L., Ding, Q., Zhong, Y., Zou, J., Wu, J., Chiu, Y. L., ... & Shen, Z. (2018). Dislocation network in additive manufactured steel breaks strength–ductility trade-off. Materials Today, 21(4), 354-361.
[11] Wang, Y. M., Voisin, T., McKeown, J. T., Ye, J., Calta, N. P., Li, Z., ... & Zhu, T. (2018). Additively manufactured hierarchical stainless steels with high strength and ductility. Nature materials, 17(1), 63-71.
[12] Bertsch, K. M., De Bellefon, G. M., Kuehl, B., & Thoma, D. J. (2020). Origin of dislocation structures in an additively manufactured austenitic stainless steel 316L. Acta Materialia, 199, 19-33.
[13] Voisin, T., Forien, J. B., Perron, A., Aubry, S., Bertin, N., Samanta, A., ... & Wang, Y. M. (2021). New insights on cellular structures strengthening mechanisms and thermal stability of an austenitic stainless steel fabricated by laser powder-bed-fusion. Acta Materialia, 203, 116476.
[14] Kong, D., Ni, X., Dong, C., Zhang, L., Man, C., Yao, J., ... & Li, X. (2018). Heat treatment effect on the microstructure and corrosion behavior of 316L stainless steel fabricated by selective laser melting for proton exchange membrane fuel cells. Electrochimica Acta, 276, 293-303.
[15] Kong, D., Dong, C., Ni, X., Zhang, L., Luo, H., Li, R., ... & Li, X. (2020). The passivity of selective laser melted 316L stainless steel. Applied Surface Science, 504, 144495.
[16] Revilla, R. I., Van Calster, M., Raes, M., Arroud, G., Andreatta, F., Pyl, L., ... & De Graeve, I. (2020). Microstructure and corrosion behavior of 316L stainless steel prepared using different additive manufacturing methods: A comparative study bringing insights into the impact of microstructure on their passivity. Corrosion Science, 176, 108914.
[17] Xiao, Q., Chen, J., Lee, H. B., Jang, C., & Jang, K. (2023). Effect of heat treatment on corrosion behaviour of additively manufactured 316L stainless steel in high-temperature water. Corrosion Science, 210, 110830.
[18] Revilla, R. I., Li, G., Pion, R., Marcoen, K., Andreatta, F., Fedrizzi, L., ... & De Graeve, I. (2024). Effect of heat treatment on the microstructure and pitting corrosion behavior of 316L stainless steel fabricated by different additive manufacturing methods (L-PBF versus L-DED): Comparative investigation exploring the role of microstructural features on passivity. Corrosion Science, 228, 111814.
[19] Pham, M. S., Solenthaler, C., Janssens, K. G. F., & Holdsworth, S. R. (2011). Dislocation structure evolution and its effects on cyclic deformation response of AISI 316L stainless steel. Materials Science and Engineering: A, 528(7-8), 3261-3269.
[20] An, D., & Zaefferer, S. (2019). Formation mechanism of dislocation patterns under low cycle fatigue of a high-manganese austenitic TRIP steel with dominating planar slip mode. International Journal of Plasticity, 121, 244-260.
[21] Prashanth, K. G., & Eckert, J. (2017). Formation of metastable cellular microstructures in selective laser melted alloys. Journal of Alloys and Compounds, 707, 27-34.
[22] An, D., Xiao, Y., Liu, X., Zhao, H., Li, X., & Chen, J. (2024). Formation of two distinct cellular structures in 316L stainless steel fabricated by micro-laser beam powder-bed-fusion. Materials Research Letters, 12(1), 42-49.
[23] Zhou, Y., Chen, K., Ferreirós, P. A., Gao, D., Song, M., Shen, Z., ... & Zeng, X. (2025). Printed cellular structure enhancing re-passivation of stress corrosion cracking in high-temperature water. Corrosion Science, 244, 112636.
[24] Beke, D. L., Erdélyi, Z., & Parditka, B. (2011, February). Effect of diffusion induced driving forces on interdiffusion-Stress development/relaxation and kinetics of diffusion processes. In Defect and Diffusion Forum (Vol. 309, pp. 113-120). Trans Tech Publications Ltd.
[25] Benabou, L. (2019). Coupled stress-diffusion modelling of grain boundary segregation and dynamic embrittlement in a copper alloy. Modelling and Simulation in Materials Science and Engineering, 27(4), 045007.
[26] Lou, X., Song, M., Emigh, P. W., Othon, M. A., & Andresen, P. L. (2017). On the stress corrosion crack growth behaviour in high temperature water of 316L stainless steel made by laser powder bed fusion additive manufacturing. Corrosion Science, 128, 140-153.
[27] Dong, P., Vecchiato, F., Yang, Z., Hooper, P. A., & Wenman, M. R. (2021). The effect of build direction and heat treatment on atmospheric stress corrosion cracking of laser powder bed fusion 316L austenitic stainless steel. Additive Manufacturing, 40, 101902.
[28] Que, Z., Riipinen, T., Goel, S., Revuelta, A., Saario, T., Sipilä, K., & Toivonen, A. (2023). SCC behaviour of laser powder bed fused 316L stainless steel in high-temperature water at 288° C. Corrosion Science, 214, 111022.
[29] Zhang, S., Wang, S., Feng, X., Ning, Z., Hou, J., & Kuang, W. (2023). Insights into the stress corrosion cracking resistance of a selective laser melted 304L stainless steel in high-temperature hydrogenated water. Acta Materialia, 244, 118561.
[30] Wang, J., Wu, Y., Zhu, T., Chen, K., Mei, J., Xue, F., ... & Zhang, L. (2023). Effect of thermal aging on the environmental assisted cracking behavior of 308L weld metal in high temperature water. Corrosion Science, 211, 110902.